Supplementary material to accompany the manuscript, "Redox variations in HSDP2 Mauna Kea lavas, the oxygen fugacity of the Hawaiian plume, and the role of volcanic gases in Earth's oxygenation" by M. Brounce, E. Stolper, and J. Eiler.

METHODS

Fe XANES

We determined $Fe^{3+}/\Sigma Fe$ ratios of pillow glass by micro-x-ray absorption near-edge structure (μ-XANES) spectroscopy at beamline 13-IDE, Advanced Photon Source, Argonne National Laboratory. Spectra were collected in fluorescence mode from 7020 eV to 7280 eV using a Si [111] monochromator and a defocused beam diameter of 50x50 μm. Counts were recorded on a multi-element silicon drift detector x-ray spectrometer, equipped with two Si drift diode detectors. Eight layers of aluminum foil were placed in the path of the incident photon beam in order to decrease the intensity of the incident photon beam prior to interaction with the surface sample, which could lead to auto-oxidation or auto-reduction of Fe species dissolved in the glass. The incident photon beam intensity resulted in on the order of 10^9-10^{10} counts on Fe on a LW standard glass (1).

Spectra were normalized and the pre-edge features were fit following techniques outlined by ref. 1, with some exceptions. Ref. 1 fit the pre-edge features using two background functions and two Gaussian curves to fit the Fe^{2+} and Fe^{3+} peaks, simultaneously solving for 11 curve parameters that are allowed to vary independently to produce a fit spectra by minimizing error between the fit and the data. In this study, we have attempted to minimize uncertainty or bias that may be introduced by allowing curve

parameters to vary, which might be reasonably expected to be constant. For instance, the width of the Gaussian curves should not be variable in glasses with similar compositions, but the intensities should vary as a function of the Fe^{3+}/Fe^{2+} ratio of the glass. To fix these two curve parameters and reduce the number of free parameters in the fit solution to 9, we calculated the average full-width half-maximum of both the high energy and low energy Gaussian curves for all the samples analyzed in each beam session. We then re-fit each spectrum, keeping the full-width half-maximum of both Gaussian curves fixed and equal to the average value of all samples analyzed in that session (supplementary figure 1, 2).

We use the ratio of the areas of each Gaussian curve in our calibration to $Fe^{3+}/\Sigma Fe$ ratios, instead of the centroid positions that ref. 1 used. Ref. 1 utilized beamline X26a at the National Synchrotron Lightsource I, which has been decommissioned. Although X26a and 13-IDE both have μ-XANES capabilities, the hardware and configuration of 13-IDE are sufficiently different from X26a that data collection routines and spectra handling require a modified approach. For example, there is not significant drift in monochromator energy at 13-IDE, which results in greater energy reproducibility in the absorption spectra collected over several hours in a beam session, as well as greater session-to-session reproducibility. This, in combination with other factors, results in significantly improved energy resolution in the pre-edge region for Fe spectra, even when using the Si [111] monochromator (supplementary figure 1). The consequence of this is that the Gaussian-fit pre-edge features that correspond the 1s to 3d electronic transitions in Fe^{3+} and Fe^{2+} are well defined compared to those collected earlier and render the use of the centroid positions in Fe redox calibrations less necessary than in previous works (e.g.,

ref. 2). Here, we use the ratio of the area under the higher energy Gaussian curve to the area under the lower energy Gaussian curve, because this ratio is closely related to the physical phenomenon of μ-XANES spectroscopy, and generate a calibration curve using the Fe^{3+}/Fe^{2+} ratio determined by Mossbauer spectroscopy, reported by ref. 1. We also utilize the centroid calibration described in ref. 1, and note that the choice of centroid or area ratio calibrations does not impact the calculated $Fe^{3+}/\Sigma Fe$ ratios of unknown samples meaningfully.

We performed an error analysis of the spectral fit parameters of spectra collected using the Si [111] monochromator using a bootstrap monte-carlo method. For a given spectrum, we assigned an arbitrary uncertainty on the deadtime corrected, normalized, detector measured counts on Fe per second for each data point in the pre-edge of 0.002. The units of this error are arbitrary, but we note that it is a liberal estimate based on observations over 20 beam sessions at two synchrotron facilities, including 10 sessions using the same detector array used in this study, 3 of which sessions were at the beamline used in this study. A normal distribution of data was generated for each data point in the pre-edge, with a standard deviation equal to the assigned analytical uncertainty and centroid equal to the actual measured value. A synthetic spectrum was then constructed by randomly sampling this distribution of data of each measured data point. This synthetic spectrum was fit using the same routine described above, and by ref. 1, and this was repeated 100 times for each collected spectrum. This exercise generates quantitative uncertainties for each spectral parameter, which can be propagated through the calibration to generate an uncertainty for $Fe^{3+}/\Sigma Fe$ ratios, which is +/- 0.015 (absolute). This can be compared to the empirical precision of the area ratios on the standard glasses,

which is +/- 0.01 (n = 2 spots), corresponding to an uncertainty in $Fe^{3+}/\Sigma Fe$ ratios of 0.006 (absolute).

Finally, we considered differences between spectra produced at X26a and 13-IDE that may arise due to major differences between beamlines, such as the energy of their respective electron storage rings (~2.8 GeV at NSLS-I X26a, ~7 GeV at APS 13-IDE), the storage ring sampling methods (bending magnet at X26a, insertion device at 13-IDE), and the intensity of the incident photon beam (orders of magnitude more intense at 13-IDE). The analytical facilities are sufficiently complicated at the synchrotron level that it is not practical for this study to seek to understand the nature of each of these differences, so we present an empirical comparison of spectra collected at X26a before NSLS-I decommission with spectra collected at 13-IDE (supplementary figure 3). The spectra are collected on two submarine glass chips from the Gulf of Aden (3). Following the methods presented here, the first glass chip has calculated $Fe^{3+}/\Sigma Fe$ ratios of 0.171 (NSLS) and 0.188 (APS). The second glass chip has calculated $Fe^{3+}/\Sigma Fe$ ratios of 0.163 (NSLS) and 0.174 (APS). The first glass chip has $Fe^{3+}/\Sigma Fe$ ratios that are 0.017 (absolute) more oxidized when measured at APS than at NSLS, and the second glass chip has $Fe^{3+}/\Sigma Fe$ ratios that are 0.011 (absolute) more oxidized when measured at APS than at NSLS. The origin of this offset is not clear at this time, but in order to produce a dataset that can be compared with previously collected data at NSLS-I, we "correct" $Fe^{3+}/\Sigma Fe$ ratios calculated from spectra collected at APS by subtracting 0.02 units from each sample average.

S XANES

We determined $S^{6+}/\Sigma S$ ratios of pillow glass by micro-x-ray absorption near-edge structure (μ-XANES) spectroscopy, also at beamline 13-IDE, Advanced Photon Source, Argonne National Laboratory. Spectra were collected in fluorescence mode from 2447 eV to 2547 eV, with a dwell time of two seconds on each point, using a Si [111] monochromator and a defocused beam diameter of 50x50 μm. Counts were recorded on a multi-element silicon drift detector x-ray spectrometer, equipped with two Si drift diode detectors. All analyses were done in a helium atmosphere, to avoid interaction between the incident photon beam and atmosphere. As with iron, to avoid significant beam damage during analysis, the beamline hardware was tuned so that the incident photon beam intensity was on the order of 10^9-10^{10} counts on S on the submarine MORB glass TR101-15D-8g, which has 1790 ppm S (supplementary figure 4a). Each sample was analyzed with a stationary beam in triplicate, moving the beam position for each of the three analysis spots.

In the absence of an independent method for accurately determining $S^{6+}/\Sigma S$ ratios, we follow the approach of ref. 4 to calculate $S^{6+}/\Sigma S$ ratios from our absorption spectra. We take a MORB glass with all sulfur present as S^{2-} and an experimental glass with all sulfur present as S^{6+} as our two endmember absorption spectra (supplementary figure 4a). Each unknown is fit using linear combinations of the MORB and experimental glasses. Since each of those glasses represents an endmember speciation of S, we assume that the intensity of absorption spectra features for both S^{2-} and S^{6+} respond linearly to the concentration of S^{2-} and S^{6+} dissolved in the sample glass, and report $S^{6+}/\Sigma S$ ratios equal to the mixing proportions of the endmember spectra necessary to fit each unknown spectra (supplementary figure 4b). The glasses in this study have low sulfur contents

compared to recent experimental glasses (4-6), which results in a decreased signal to noise ratio in collected spectra. We estimate that the uncertainty on these sulfur XANES measurements is +/- 0.01 (absolute), based on the reproducibility of spectra from individual natural samples.

To test the extent of possible beam damage, we collected several spectra in one location on a series of back-arc basin glasses that have spectral features indicative of the presence of both S^{2-} and S^{6+}, exposing the same pool of glass to the incident photon beam for 110 consecutive minutes (supplementary figure 5). There are noticeable changes in the sulfur absorption spectra over this time period. The S^{6+} absorption feature decreases in intensity. At the same time, the broad S^{2-} absorption feature increases in intensity, but at slightly higher energy than the center position of this feature. This could be due to the generation of S^{4-} as the result of beam damage (5, 6). The overall differences in intensity of the absorption features between spot 1 and spot 10 (i.e., after 110 minutes of beam exposure) are small, and unlikely to impact the calculated $S^{6+}/\Sigma S$ ratios determined here. Nonetheless, we collect a single spectrum in eleven minutes, and then move the position of the incident photon beam before collecting another spectrum on the same sample, limiting the exposure time of any glass pool.

VOLATILES IN HSDP2 SUBMARINE GLASS

Supplementary figure 6 shows the key relationships between S and FeO*, and S and H_2O described in the main text. The S contents of all but two glasses are below the sulfur content of MORB magmas that are sulfide-saturated, from ref. 7, modified after ref. 8. The sulfur contents range from ~200 ppm to ~1400 ppm within a narrow range of

FeO*, suggesting that sulfur degassing is taking place in a sulfide-undersaturated melt. This is supported by petrographic descriptions from ref. 8 that note these glasses do not appear to have sulfide blebs present. Both suites have H_2O and S contents that are positively correlated. The low SiO_2 glasses appear to have higher initial H_2O contents, but similar initial S contents, relative to the low SiO_2 glasses (i.e. low SiO_2 glasses have higher H_2O/S ratios than high SiO_2 glasses; supplementary figure 6b), but both suites are consistent with concomitant sulfur and water degassing.

COMPARISON TO OTHER DEGASSING-REDOX STUDIES

Supplementary figure 7 shows the relationship between $Fe^{3+}/\Sigma Fe$ ratios and calculated magmatic fO_2s, and S and H_2O contents in submarine pillow glasses from this work, and in two other recent studies of olivine hosted melt inclusions (9, 10). The Agrigan melt inclusions are more oxidized than the HSDP2 submarine glasses in this study (Supplementary Fig. 12 a-f). The Agrigan melt inclusions are also more water rich than the HSDP2 submarine glasses (Supplementary Fig. 12e). The relationship between $Fe^{3+}/\Sigma Fe$ ratios and S and H_2O contents is less systematic than is observed for HSDP2 submarine glasses (Supplementary Fig. 12 a, b). This could be because the HSDP2 submarine glasses are more restricted in their major element compositions, or because melt inclusion processes introduce variability in $Fe^{3+}/\Sigma Fe$ ratios +/- H_2O contents, +/- S contents of the Agrigan dataset, or some combination of the two. The Agrigan melt inclusions also record more oxidized magmatic fO_2s than the HSDP2 submarine glasses (Supplementary Fig. 12 d-f). The Erebus melt inclusions span a wide range in $Fe^{3+}/\Sigma Fe$ ratios and S contents, and a wider range in H_2O contents than the HSDP2 submarine

glasses, but are not as water rich as the Agrigan melt inclusions (Supplementary Fig. 12 a, b, d, e). The relationship between $Fe^{3+}/\Sigma Fe$ ratios and S and H_2O contents in Erebus melt inclusions are less systematic than the submarine glasses from this study, similarly to the Agrigan melt inclusions (Supplementary Fig. 12 a, b). The general sense of decreasing $Fe^{3+}/\Sigma Fe$ ratios with increasing extents of degassing is broadly similar between the three datasets, despite differences in sample types (i.e., submarine glass vs. olivine-hosted melt inclusions), magma compositions, and magma storage conditions (Supplementary Fig. 12 a, b). The extent of reduction per ppm S loss (or per wt% H_2O lost) is greatest for Erebus melt inclusions and HSDP2 submarine glasses (i.e., the slope of the relationship between S and H_2O and $Fe^{3+}/\Sigma Fe$ ratios is steepest for these samples; Supplementary Fig. 12 a).

MODELING THE IMPACT OF DEGASSING ON MELT fO_2

We modeled the change in magmatic fO_2 with progressive degassing of a C-O-H-S vapor species using the gas-melt equilibrium model of ref. 11. This thermodynamic model computes C, H, O, and S concentrations and speciation in coexisting fluid (i.e., gas) and silicate melt as functions of pressure, temperature, and fO_2, based on experimental calibrations of melt solubility and homogeneous equilibrium in the gas phase for H_2, H_2O, CO, CO_2, SO_2, H_2S, and S_2 species. The melt is assumed in this model not to crystallize any solids or to precipitate a separate sulfide phase. We modified the solubility models of ref. 11 so that they fit the experimental results of ref. 12 for H_2O and CO_2 solubility. In Figure 3a and b, the calculation begins at a total pressure of 120 bar, a temperature of 1190°C, and an fO_2 for the initial (i.e., undegassed) melt (QFM+1.1) that

is slightly higher than the highest fO_2 constraint from this study; the volatile contents of the initial melt were set at 1.05 wt% H_2O, 1370 ppm S, and 0 ppm CO_2, near the highest volatile contents measured in the samples from this study (except for the assumed zero concentration of CO_2; if the initial melt is allowed to have CO_2 at the 100-200 ppm level, the model curves predict less total reduction in fO_2). We assume the melt has the major element composition of sample SR0914-10.50, a high-SiO_2 glass with high S content (1370 ppm S). The modeling assumes that the initial melt is vapor saturated at the starting pressure and temperature of the calculation. We calculated redox conditions and coexisting vapor and silicate liquid compositions by progressively decreasing total pressure (at a constant temperature of 1190°C) from the assumed starting pressure of 120 bars down to 1 bar both for fractional (red curve, Fig. 3a, b) and batch (blue curve, Fig. 3a, b) degassing.

Supplementary figure 8 shows the relationship between gas phase and melt redox defined by the degassing models used in the main text. We show degassing trajectories for a melt containing H_2O as the only volatile element (gray long dashed line, Supplementary Fig. 8), a melt containing S as the only volatile element (solid gray line, Supplementary Fig. 8), a melt containing CO_2 as the only volatile element (dash-dot gray line, Supplementary Fig. 8), a melt containing both H_2O and S (short dashed gray line, Supplementary Fig. 8), and a melt containing H_2O, S, and CO_2 (solid black line, Supplementary Fig. 8).

It is possible (and indeed likely for CO_2; e.g., ref. 13) that the least degassed of our samples were themselves the degassing products of more volatile-rich liquids. In principle, the original magmatic fO_2 before degassing from such melts could be estimated

by incrementally adding the composition of the saturating vapor to the least degassed melt composition, calculating the fO_2 of this volatile-enriched melt and finding the pressure at which it is vapor saturated, and then repeating this up to arbitrarily high volatile contents and pressures. However, the most volatile-rich glasses in this study are approximately saturated with a liquid sulfide phase based both on thin section study and their position on an Fe-S plot for basaltic melts (Supplementary Fig. 6a; refs. 7, 8). Degassing (or the addition of gas to) a melt containing sulfide blebs cannot be as simply modeled as degassing from a sulfide under-saturated melt. For example, when on decompression, S transfers from the silicate liquid to a vapor phase, the silicate liquid would respond by dissolving a fraction of the sulfide phase in order to maintain the appropriate sulfur content at sulfide saturation. This not only would tend to buffer the S content of the melt even while degassing proceeds, but it would likely increase the FeO* content of the melt (which in turn would influence the sulfide solubility) and would therefore have feedback on fO_2. These processes have not, to our knowledge, been quantitatively modeled, and they are beyond the scope of this study. Consequently, we have not explored any degassing history and fO_2 for liquids more volatile-rich than the HSDP2 samples with the highest S and H_2O contents.

IMPACT OF PRESSURE AND TEMPERATURE ON SILICATE MELT fO_2 RELATIVE TO QFM

The mantle source for Hawaiian magmas undergoes melting at higher pressure and temperatures than the mantle source for mid-ocean ridge magmas. We calculated the effect that this will have on absolute fO_2 calculated from $Fe^{3+}/\sum Fe$

ratios, as well as fO_2 relative to the QFM oxygen buffer, using the algorithm of ref. 14 and the definition of the QFM oxygen buffer according to ref. 15. Supplementary figure 9 shows the results of these calculations, and demonstrates that increasing pressure from 1 to 3 GPa causes an increase in the absolute fO_2 of both silicate melt and the QFM oxygen buffer, but that the absolute fO_2 of the silicate melt increases slightly more than that of QFM, leading to a change in fO_2 relative to QFM of ~0.14 log units for the silicate melt at 3 GPa. The opposite is true for a silicate melt at higher temperature. The difference in absolute fO_2 between a silicate melt and QFM decreases with increasing temperature by <0.02 log unit from 1200°C to 1400°C. We conclude that the higher pressures and temperatures of equilibration for primary melts in Hawaii can account for ~0.13 log units of the observed offset between the fO_2 of undegassed Hawaiian melts and undegassed MORB.

THE EFFECT OF OLIVINE REMOVAL ON Fe REDOX

Hawaiian primary magmas are thought to be in equilibrium with Fo90-Fo91 olivine, and as a result, likely crystallize significantly higher mass fraction of olivine prior to eruption than MORB magmas at the same MgO content. We calculated the $Fe^{3+}/\sum Fe$ ratios and fO_2 of primary mantle melts for MOR and Hawaiian settings by taking an undegassed composition from each setting and adding the equilibrium composition olivine back to the melt in 0.1% increments, treating Fe^{2+} and Fe^{3+} as conservative elements (Supplementary Fig. 10). We use a $K_D^{Fe2+/Mg}$ between olivine and melt of 0.34. We recalculate the equilibrium olivine composition at each increment, and continue the calculation until the melt composition is in equilibrium with Fo89, Fo90,

and Fo91 olivine. A MORB primary melt in equilibrium with Fo90 olivine has 16 wt% MgO, 0.12 $Fe^{3+}/\sum Fe$, and has fO_2 ~QFM-0.3. A Hawaiian primary melt with the same $Fe^{3+}/\sum Fe$ ratio and fO_2 is in equilibrium with Fo93.5 olivine and has 26 wt% MgO, both of which are considered too high to be reasonable for Hawaiian mantle and melts. If Hawaiian primary melts are in equilibrium with Fo91 olivine, they have 19 wt% MgO, 0.14 $Fe^{3+}/\sum Fe$, and fO2 ~QFM+0.2. We conclude that the difference in primary melt compositions between Hawaii and MOR settings can account for ~0.5 log units of the observed offset between undegassed Hawaiian and MORB melts.

FIGURE CAPTIONS

Figure 1. A stacked plot of pre-edge features on the same standard glass, analyzed at beamline X26a at NSLS (light gray line) and beamline 13-IDE at APS (black line). The spectrum at NSLS was collected using a Si [311] monochromator. The spectrum at APS was collected using a Si [111] monochromator.

Figure 2. A plot of a pre-edge feature from standard glass LW-0 and the fit parameters, obtained using the methods described here.

Figure 3. A comparison of $Fe^{3+}/\Sigma Fe$ ratios calculated from spectra collected on the same glasses from APS and NSLS, using area ratio calibrations described here. Error bars represent the uncertainty on spectral fits using the monte carlo boot strap simulation described here.

Figure 4. Sulfur absorption spectra of (a) endmember composition glasses, and (b) unknown HSDP2 glass SR0915-0.4.The red dashed line in panel b represents the fit to the unknown data, obtained using linear combinations of the spectra in panel a.

Figure 5. Two sulfur absorption spectra demonstrating the effects of beam damage on the intensity of the S^{6+} absorption feature.

Figure 6. Plots of S versus (a) FeO* concentrations, and (b) H_2O concentrations in HSDP2 submarine glasses. The dark black line in panel a is the sulfur concentrations in MORB that are sulfide saturated, from Mathez et al. (1974) and modified from Seaman et al. (2004).

Figure 7. (a) Fractional (black curve) and batch (gray curve) degassing calculations as in (Fig. 3a, b main text), where H_2O is assumed to be the only volatile component dissolved in the melt in order to isolate the effects of degassing of H_2O from melts from those of S and CO_2. White circles are submarine glass and melt inclusions from Mariana arc volcanoes (7), gray circles are submarine glass from the Mariana Trough back-arc spreading center (7), and black circles are submarine MORB glasses (44). (b) Fractional (black curve) and batch (gray curve) degassing calculations as in (a), where S is assumed to be the only volatile component in the melt in order to isolate the effects of degassing of S from melts from those of H_2O and CO_2.

Figure 8. Plot of magmatic fO_2 versus pressure for several batch degassing trajectories, using the D-COMPRESS algorithm presented by Burgisser et al. (2015).

Figure 9. Plots of (a) pressure and (b) temperature versus fO_2 for silicate melts (squares and inverted triangles) and the QFM oxygen buffer (solid and dashed black lines). The fO_2 is calculated according to Kress and Carmichael (1991) and QFM is defined according to Frost (1991).

Figure 10. Plot of $Fe^{3+}/\Sigma Fe$ ratios versus MgO concentration for submarine glasses from MORB (Cottrell and Kelley; 2011) and HSDP-2 (this study). Calculations show olivine addition trajectories for undegassed MORB and HSDP-2 samples, with endpoints at melts in equilibrium with Fo89, Fo90, and Fo91 olivine.

Figure 11. Plots with the results of fractional degassing models calculated using the D-COMPRESS software from Burgisser et al. (2015), showing pressure (bars) versus (a) fO_2 of the melt, and (b, c) the Holland *f* factor of the gas phase. The solid black curves represent modern degassing scenarios from OIB (stars, same degassing model from Fig. 3a, b, for HSDP2 glasses), MORB (circles; initial melt has fO_2 = QFM+0.3, 0.1 wt% H_2O, 200 ppm CO_2, 1700 ppm S), and arc (triangles, initial melt has fO_2 = QFM+1.5, 4.5 wt% H_2O, 800 ppm CO_2, 1982 ppm S) settings. All models assume no sulfide phase is allowed to precipitate. We use the same solubility models as for the HSDP2 models described in the text. The curve for MORB degassing extends to 1 bar pressure, however the average pressure of MORB eruptions is 300 bars (marked with a horizontal gray line

on all panels to demonstrate the melt and gas phase chemistries of MORB magmas on eruption to the seafloor). The arc degassing curve approximates the trend in volatile contents and fO_2 of melt inclusions from Agrigan volcano in the Mariana arc (Kelley and Cottrell, 2012). The gray curve is a fractional degassing scenarios for a reduced (initial melt has fO_2 = QFM-2.3, 0.75 wt% H_2O, 250 ppm CO_2, 2500 ppm S) basaltic magma. The *f* factor is calculated from the output gas chemistries from the D-COMPRESS software of Burgisser et al. (2015), as in equation 1 from the text.

Figure 12. Plots of $Fe^{3+}/\Sigma Fe$ ratios versus (a) sulfur concentrations, (b) H_2O concentrations, (c) total Fe expressed as FeO, and calculated magmatic fO2 relative to QFM versus (d) sulfur concentrations, (e) H_2O concentrations, (f) total Fe expressed as FeO in HSDP2 submarine glasses and olivine hosted melt inclusions from Moussallam et al. (2014, black squares) and Cottrell and Kelley (2012, white squares). Calculated fO_2 for Agrigan and Erebus magmas are taken directly from the original publications. The fO_2s for HSDP2 submarine glasses are calculated at 1200 C and 1 atm according to the algorithm of Kress and Carmichael (1991) relative to the position of the quartz-fayalite-magnetite oxygen buffer according to Frost (1991).

REFERENCES CITED

1. Cottrell, E, Kelley, K. A, Lanzirotti, A, Fischer, R. A (2009) High-precision determination of iron oxidation state in silicate glasses using XANES. *Chem Geol* 268: 167-179, doi:10.1016/j.chemgeo.2009.08.008.
2. Berry, A.J, O'Neill, H.S.C, Jayasuria, K.D, Campbell, S.J, Foran, G.J (2003) XANES calibrations for the oxidation state of iron in a silicat glass. *Am Mineral* 88(7): 967-977.
3. Kelley, K. A, Kingsley, R, Schilling, J.-G (2013) Composition of plume-influenced mid-ocean ridge lavas and glasses from the Mid-Atlantic Ridge,

East Pacific Rise, Galápagos Spreading Center, and Gulf of Aden. *Geochem Geophys Geosys* 14: 223-242, doi:10.1002/ggge.20049.
4. Jugo, P. J, Wilke, M, Botcharnikov, R. E (2010) Sulfur K-edge XANES analysis of natural and synthetic basaltic glasses: Implications for S speciation and S content as function of oxygen fugacity. *Geochim Cosmochim Act* 74: 5926-5938, doi:10.1016/j.gca.2010.07.022.
5. Klimm, K, Kohn, S. C, O'Dell, L. A, Botcharnikov, R. E, Smith, M. E (2012) The dissolution mechanism of sulphur in hydrous silicate melts. I: Assessment of analytical techniques in determining the sulphur speciation in iron-free to iron-poor glasses. *Chem Geol* 322-323: 237-249, doi:10.1016/j.chemgeo.2012.04.027.
6. Klimm, K, Kohn, S. C, Botcharnikov, R. E (2012) The dissolution mechanism of sulphur in hydrous silicate melts. II: Solubility and speciation of sulphur in hydrous silicate melts as a function of fO_2. *Chem Geol* 322-323: 250-267, doi:10.1016/j.chemgeo.2012.04.028.
7. Mathez, E.A (1976) Sulfur solubility and magmatic sulfides in submarine basalt glass. *J Geophys Res* 81: 4269-4276.
8. Seaman, C, Sherman, S.B, Garcia, M.O, Baker, M.B, Balta, B, Stolper, E (2004) Volatiles in glasses from the HSDP2 drill core. *Geochem Geophys Geosys* 5: doi:10.1029/2003GC000596.
9. Moussallam, Y, Oppenheimer, C, Scaillet, B, Gaillard, F, Kyle, P, Peters, N, Hartley, M, Berlo, K, & Donovan, A (2014) Tracking the changing oxidation state of Erebus magmas, from mantle to surface, driven by magma ascent and degassing. *Earth Planet Sci Lett* 393: 200-209.
10. Kelley, K, Cottrell, E (2012) The influence of magmatic differentiation on the oxidation state of Fe in a basaltic arc magma. *Earth Planet Sci Lett* 329: 109-121.
11. Burgisser, A, Alletti, M, Scaillet, B (2015) Simulating the behavior of volatiles belonging to the C–O–H–S system in silicate melts under magmatic conditions with the software D-Compress. *Comps Geosc* 79: 1-14, doi:10.1016/j.cageo.2015.03.002.
12. Dixon, J.E, Stolper, E.M, Holloway, J.R (1995) An experimental study of water and carbon dioxide solubilities in mid-ocean ridge basaltic liquids. Part I: Calibration and solubility models. *J Petrol* 36(6): 1607-1631.
13. Gerlach, T.M, Graeber, E.J (1985) The volatile budget of Kilauea volcano. *Nature* 313: 273-277.
14. Kress, V. C, Carmichael, I. S. E (1991) The compressibility of silicate liquids containing Fe2O3 and the effect of composition, temperature, oxygen fugacity and pressure on their redox states. *Contrib Mineral Petrol* 108: 82-92.
15. Frost, B. R (1991) Introduction to oxygen fugacity and its petrologic importance. *Rev Mineral Geochem* 25: 1-9.

Supplementary Figure 1

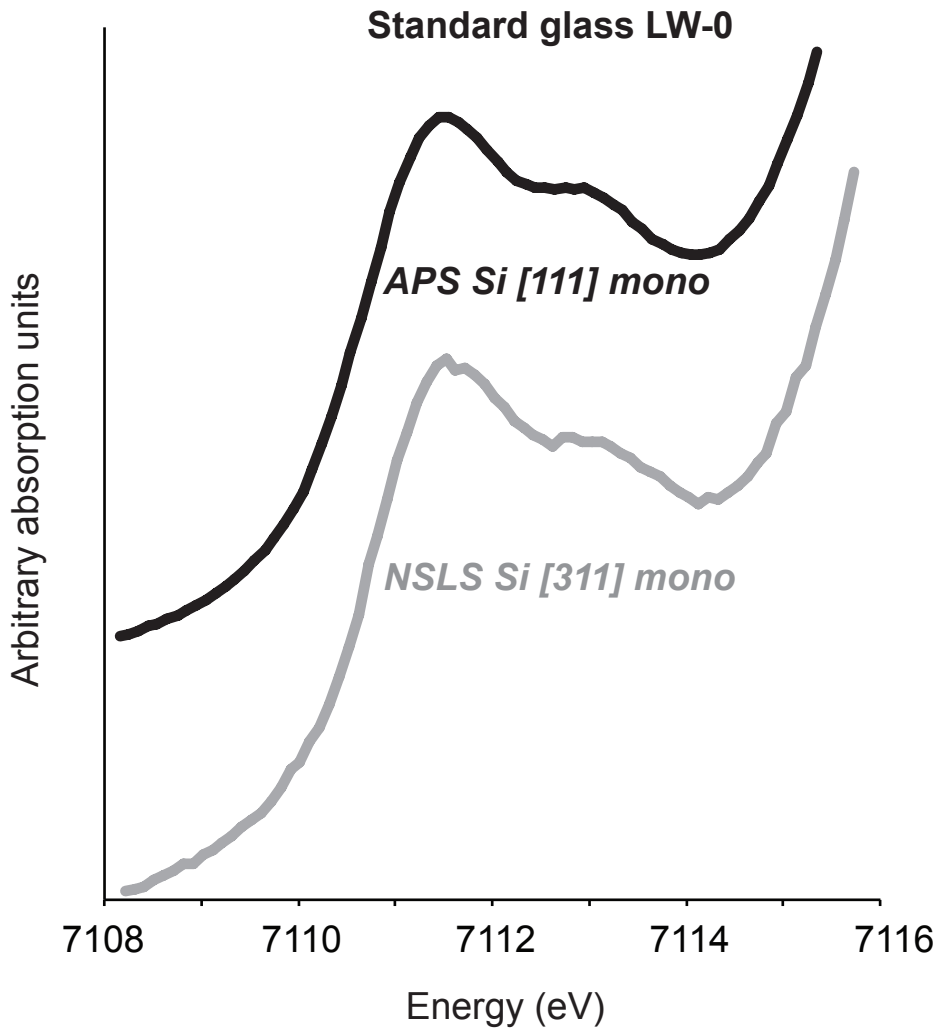

Supplementary Figure 2

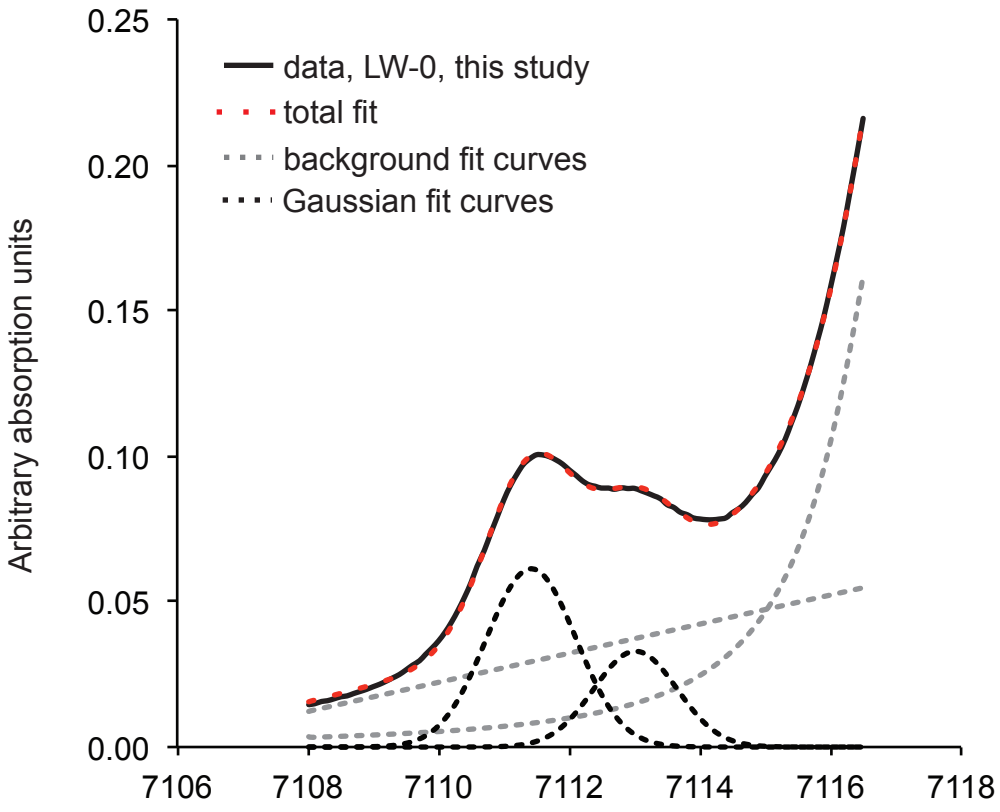

Supplementary Figure 3

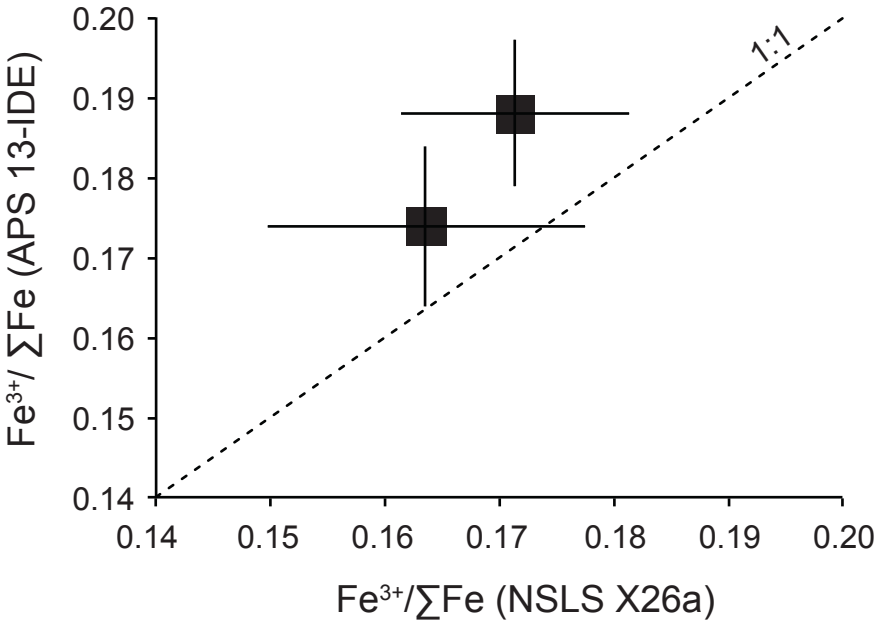

Supplementary Figure 4

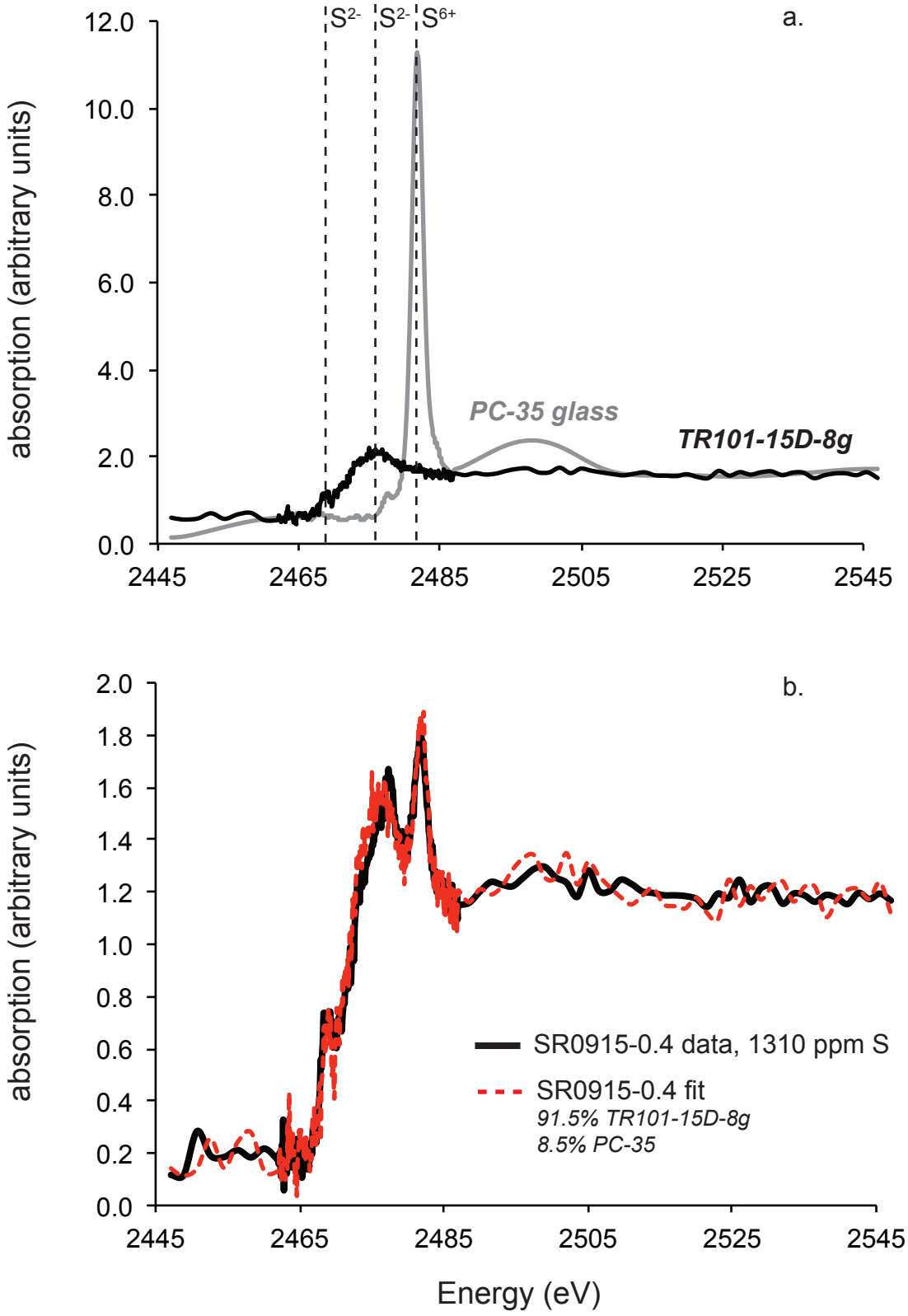

Supplementary Figure 5

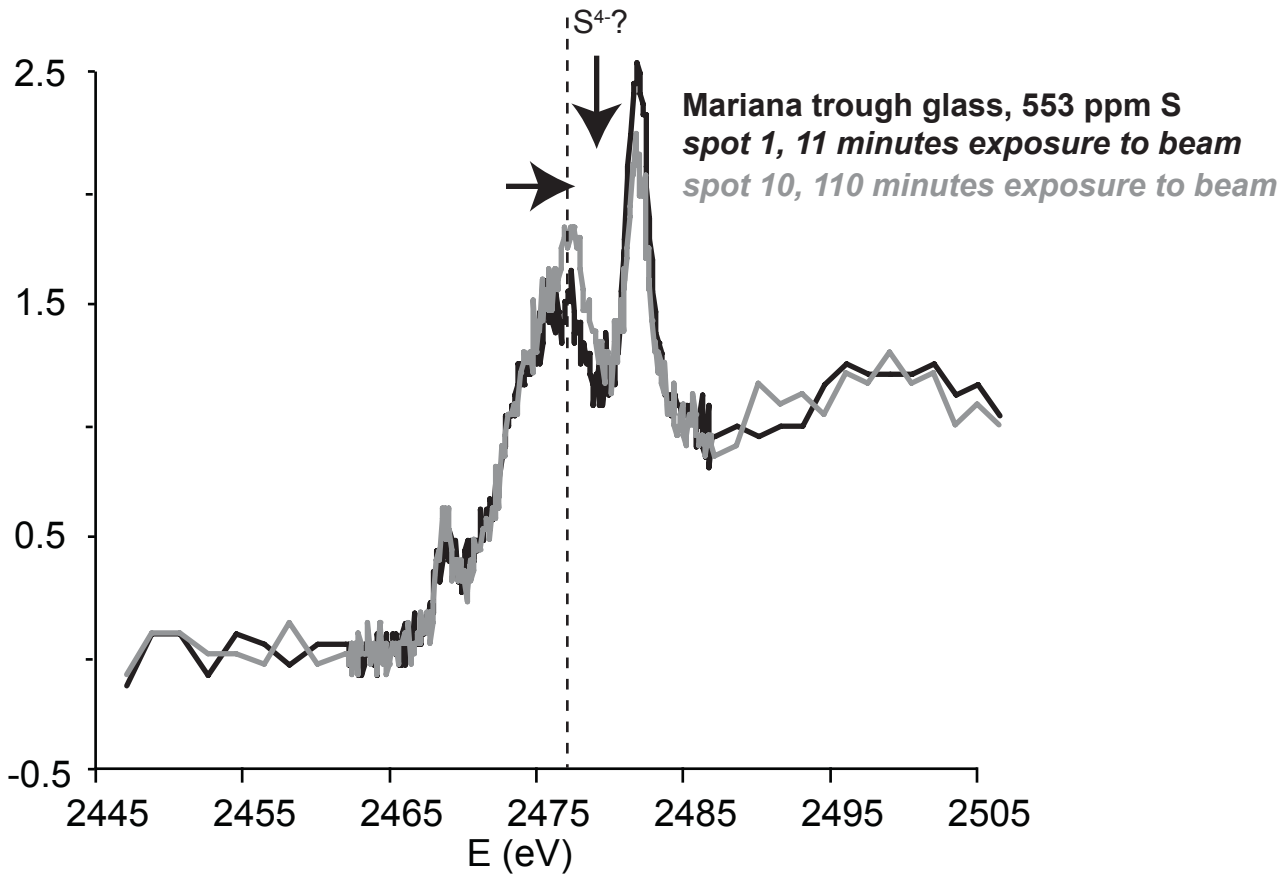

Supplementary Figure 6

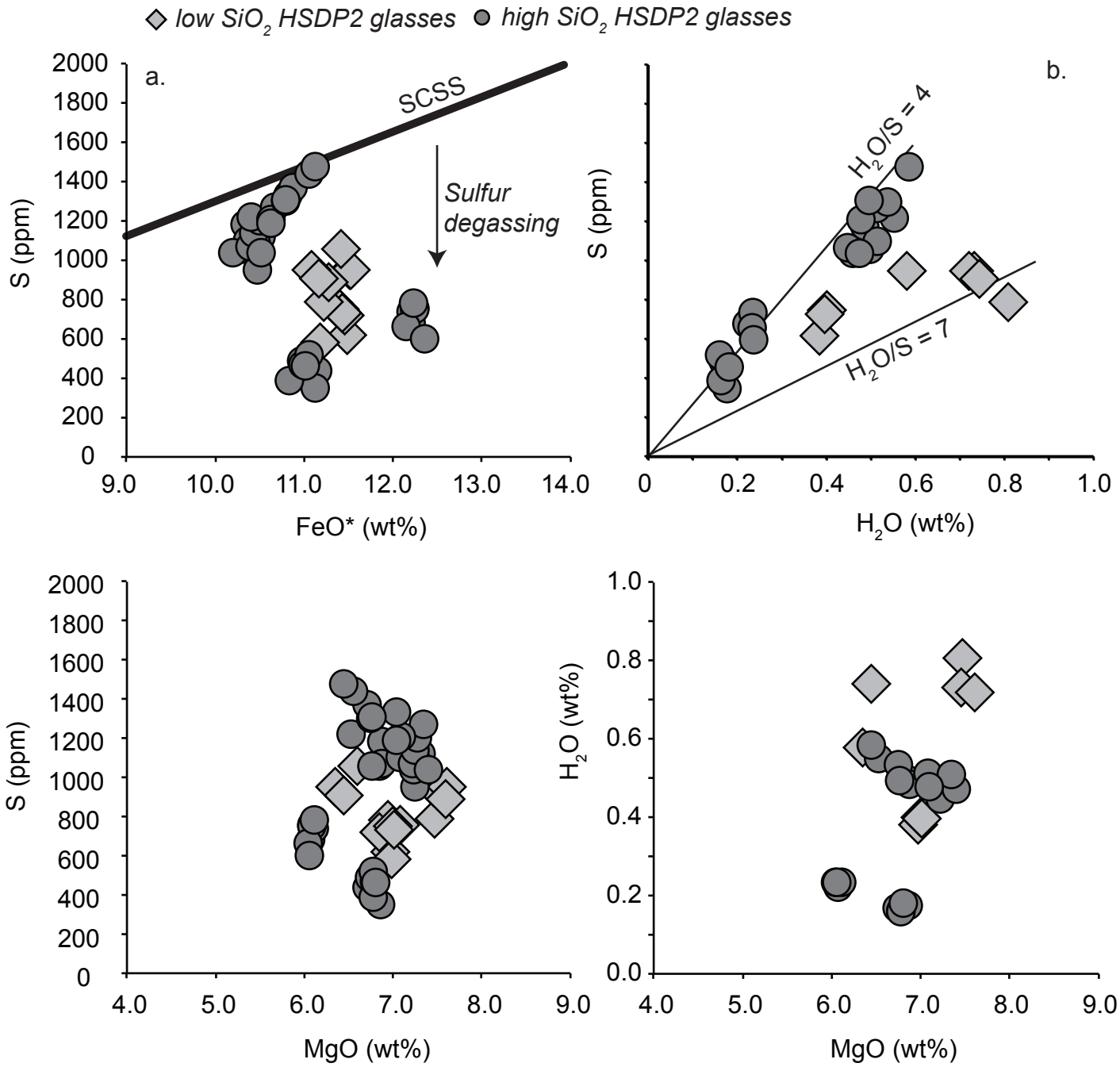

Supplementary Figure 7

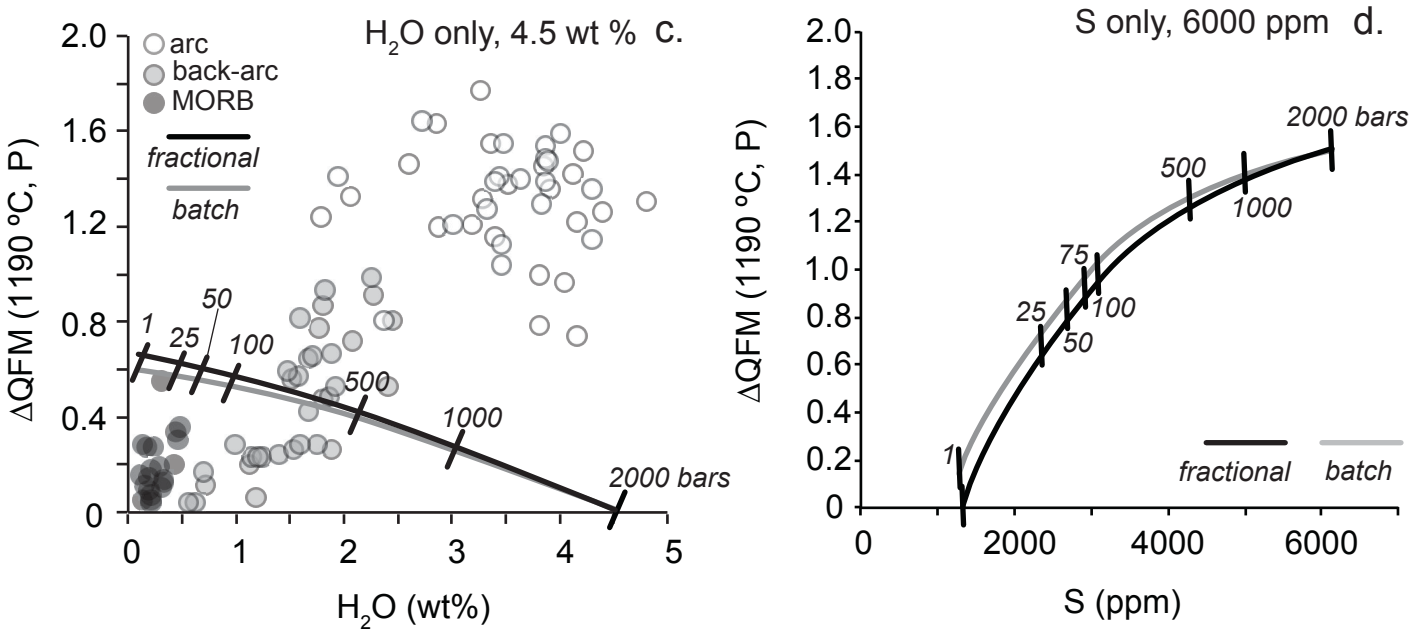

Supplementary Figure 8

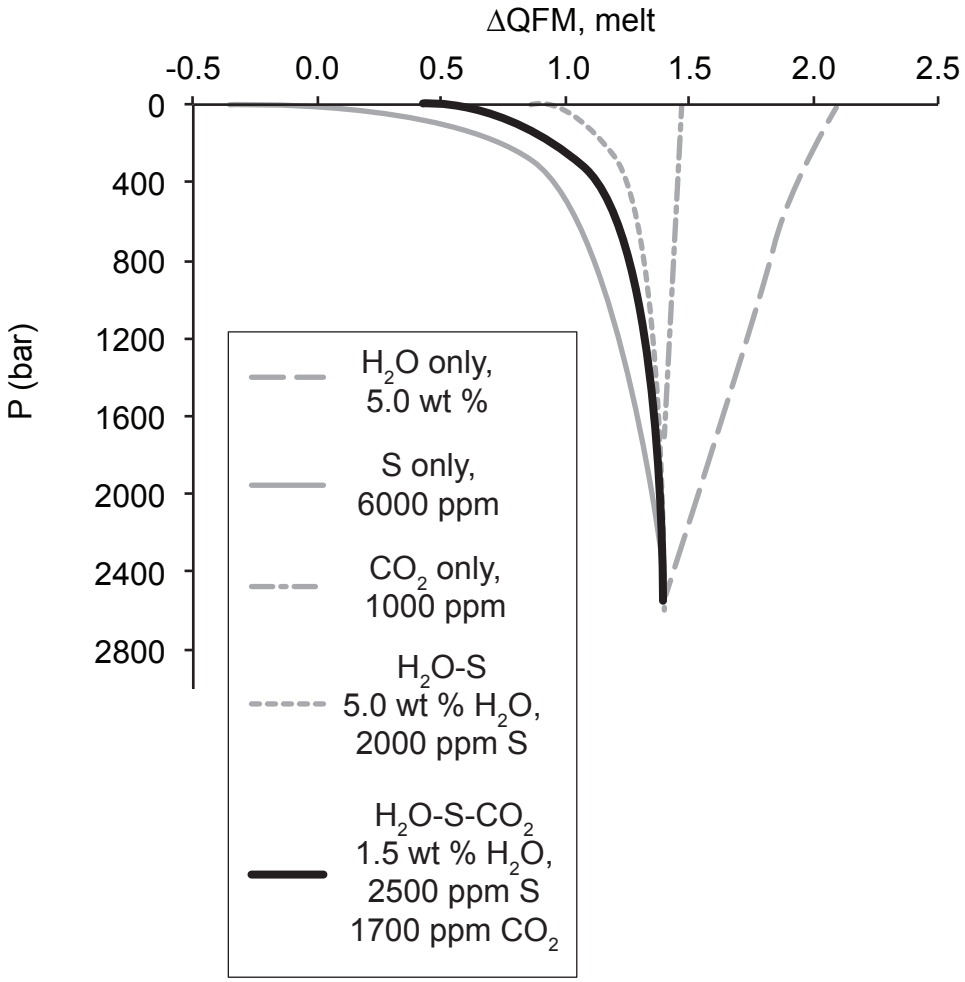

Supplementary Figure 9

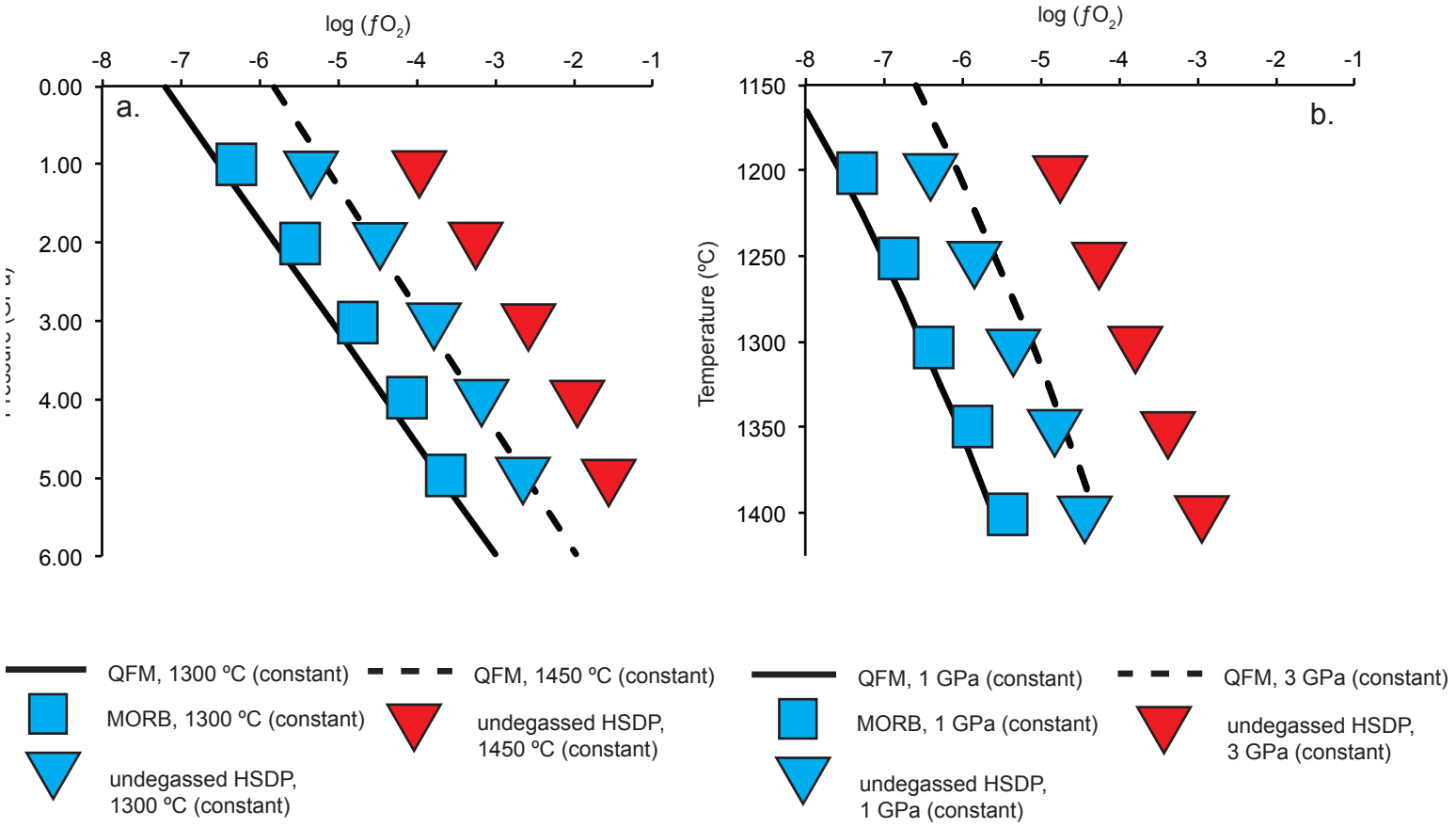

Supplementary Figure 10

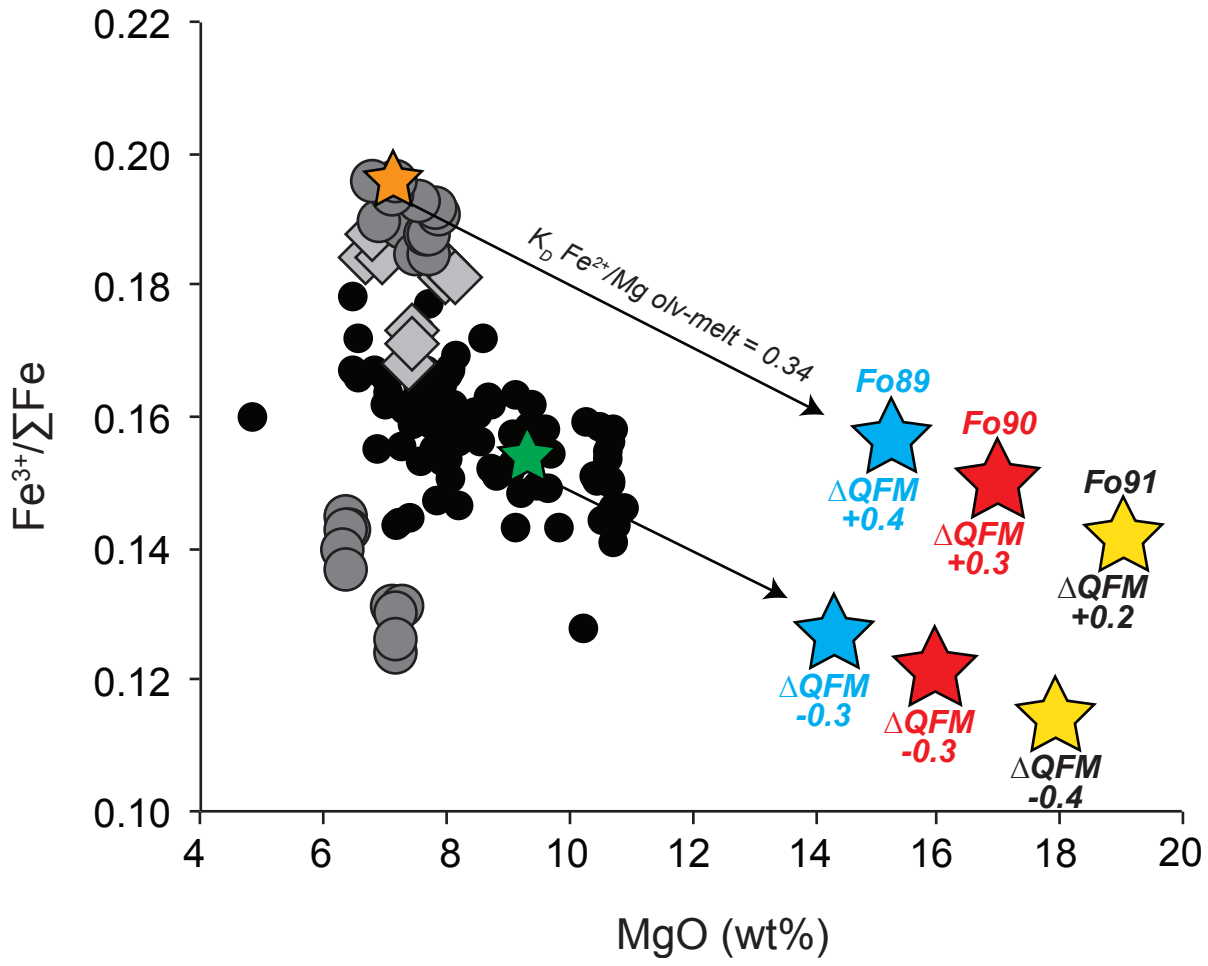

Supplementary Figure 11

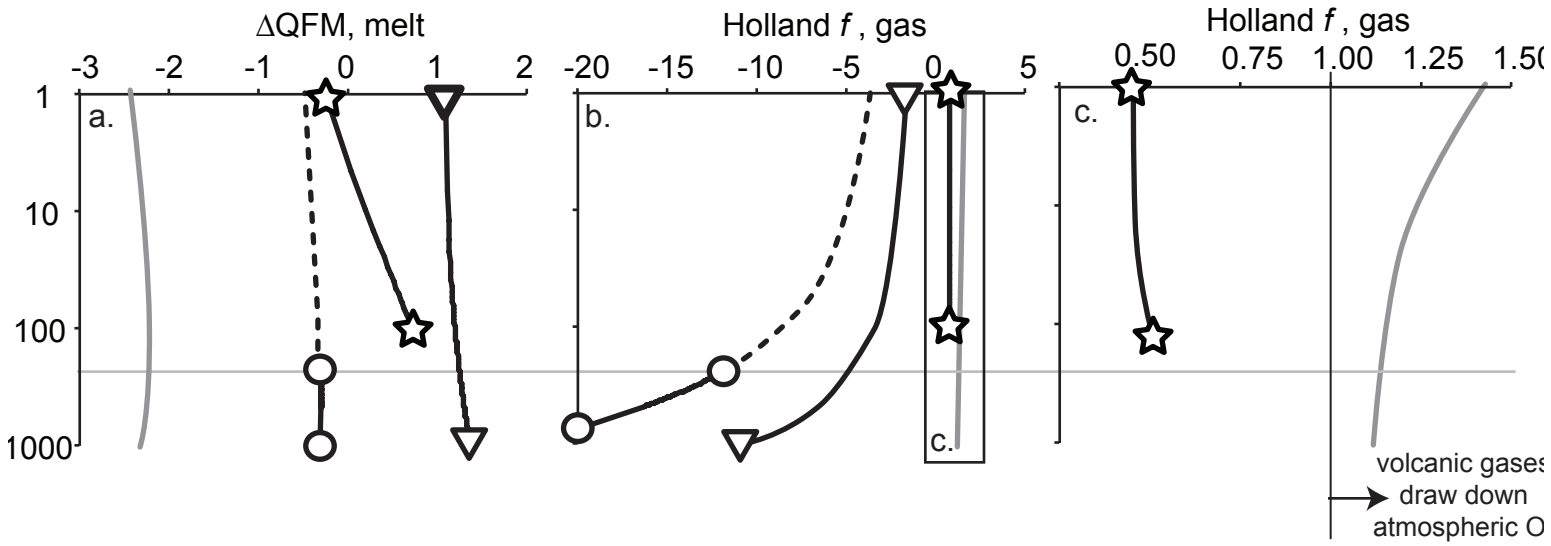

HSDP2 degassing

MORB degassing

Arc degassing

Hypothetical degassing scenario
QFM-2.3

$CO_2^{melt,init}$ = 250 ppm

$S^{melt,init}$ = 2500 ppm

$H_2O^{melt,init}$ = 0.75 wt%

Supplementary Figure 12